Selective high-temperature CO2 electrolysis enabled by oxidized carbon intermediates

Skafte, Theis L.; Guan, Zixuan; Machala, Michael L. ; Gopal, Chirranjeevi B. ; Monti, Matteo ; Martinez, Lev; Stamate, Eugen; Sanna, Simone; Garrido Torres, Jose A.; Crumlin, Ethan J.

Total number of authors:
14

Published in:
Nature Energy

Link to article, DOI:
10.1038/s41560-019-0457-4

Publication date:
2019

Document Version
Peer reviewed version

Selective high-temperature CO_2 electrolysis enabled by oxidized carbon intermediates

Theis L. Skafte[1,2,3,4], Zixuan Guan[5], Michael L. Machala[2], Chirranjeevi B. Gopal[2], Matteo Monti[2], Lev Martinez[1], Eugen Stamate[1], Simone Sanna[1], Jose A. Garrido Torres[3], Ethan J. Crumlin[6], Max García-Melchor[7], Michal Bajdich[3 *], William C. Chueh[2,8 *] and Christopher Graves[1,2,3 *]

[1]Department of Energy Conversion and Storage, Technical University of Denmark, Risø campus, Frederiksborgvej 399, 4000 Roskilde, Denmark.

[2]Department of Materials Science and Engineering, Stanford University, 496 Lomita Mall, Stanford, CA 94305, USA.

[3]SUNCAT Center for Interface Science and Catalysis, SLAC National Accelerator Laboratory, 2575 Sand Hill Road, Menlo Park, CA 94025, USA.

[4]Haldor Topsoe A/S, Haldor Topsøes Allé 1, 2800 Kgs. Lyngby, Denmark.

[5]Department of Applied Physics, Stanford University, 348 Via Pueblo Mall, Stanford, CA 94305, USA.

[6]Advanced Light Source, Lawrence Berkeley National Laboratory, 1 Cyclotron Road, Berkeley, CA 94720, USA.

[7]School of Chemistry, CRANN and AMBER Research Centres, Trinity College, College Green, Dublin 2, Ireland.

[8]Stanford Institute for Materials and Energy Sciences, SLAC National Accelerator Laboratory, 2575 Sand Hill Road, Menlo Park, CA 94025, USA.

*Correspondence to: cgra@dtu.dk, wchueh@stanford.edu, and bajdich@slac.stanford.edu

Abstract: High-temperature CO_2 electrolyzers offer exceptionally efficient storage of renewable electricity in the form of CO and other chemical fuels, but conventional electrodes catalyze destructive carbon deposition. Ceria catalysts are known carbon inhibitors for fuel cell (oxidation) reactions, however for the more severe electrolysis (reduction) conditions, catalyst design strategies remain unclear. Here we establish the inhibition mechanism on ceria and show selective CO_2 to CO conversion well beyond the thermodynamic carbon deposition threshold. Operando X-ray photoelectron spectroscopy during CO_2 electrolysis – using thin-film model electrodes consisting of samarium-doped ceria, nickel, and/or yttria-stabilized zirconia – together with density functional theory modeling reveal the crucial role of oxidized carbon intermediates in preventing carbon buildup. Using these insights, we demonstrate stable electrochemical CO_2 reduction with a scaled-up 16 cm^2 ceria-based solid oxide cell under conditions that rapidly destroy a nickel-based cell, leading to substantially improved device lifetime.

Main Text: CO_2 utilization is expected to play a key role in achieving a carbon-neutral sustainable energy economy. Electrochemical CO_2 reduction, in particular, is a promising way to store intermittent electricity derived from solar and wind in the form of chemicals, such as synthetic hydrocarbons compatible with the existing energy infrastructure, and is therefore an essential technology in decarbonization strategies [1–4]. Currently, the most efficient CO_2 electrolysis technology is the elevated-temperature solid oxide electrochemical cell (SOC), which utilizes O^{2-} as the mobile ion. SOCs produce CO and O_2 at the thermoneutral voltage of ~1.46 V with current densities exceeding 1 A/cm^2 – similar to steam electrolysis, which can be carried out simultaneously in the same cell to produce syngas or methane [1,2,5,6]. The same SOC can be operated in reverse as a fuel cell to re-oxidize the fuel products, thereby enabling operation as a flow battery [6,7]. Another important application is O_2 (and CO) production from the CO_2-rich atmosphere of Mars for rocket propulsion and life support, which will be demonstrated on the NASA Mars 2020 rover [8].

A key challenge for CO_2 electrolysis in SOCs is the competition between CO generation ($2CO_2(g) \rightarrow 2CO(g) + O_2(g)$) and C deposition ($CO_2(g) \rightarrow C + O_2(g)$) [8–10]. In technologically-relevant SOCs, Ni is the most commonly employed electrocatalyst in the fuel electrode (typically as a porous composite with yttria-stabilized zirconia, YSZ). Unfortunately, Ni is also an excellent catalyst for destructive carbon formation [11] during electrolysis, which eventually fractures the porous electrode [9,10,12]. The global thermodynamics of carbon formation are understood in terms of CO disproportionation, also known as the Boudouard reaction ($2CO(g) \rightleftharpoons C + CO_2(g)$), which is obtained by subtracting the two aforementioned reactions [8,9,13], see Supplementary Note 1. Boudouard deposition is also a concern in fuel cell mode, albeit with much less severity than in electrolysis due to the oxidizing environment [14,15]. Advanced carbon-tolerant fuel cell electrodes almost universally include $CeO_{2-\delta}$ (ceria, substituted with trivalent cations such as Sm and Gd), or other oxygen-storing oxides, as an active component [16–22]. It was recently proposed that carbon tolerance on ceria in fuel cells could also extend to electrolysis cells [10].

Rational design rules for these carbon-resistant electrode materials have been largely inferred from studies on carbon deposition during steam reforming in heterogeneous catalysis [15,23,24]. For example, density functional theory (DFT) calculations showed that adsorbed oxidized carbon species provide an inhibiting effect on the deposition of carbon on terraces and steps in heterogeneous catalysts [25,26], and it was suggested that increasing their formation rate will increase the carbon tolerance [15]. Participation of carbonate species in hydrocarbon oxidation in solid-oxide fuel cells was investigated using Raman spectroscopy, suggesting that carbonate oxidizes deposited carbon into adsorbed carbon groups [19]. Nevertheless, CO_2 electrolysis in SOCs is fundamentally distinct from these processes. For example, under high conversion conditions, $CO_2(g)$ and $CO(g)$ are present in significant concentrations, which directly affects the coverage of reaction intermediates on the electrode surface. Moreover, the surface oxygen activity is controlled by the electrode overpotential, again influencing the rates of $CO(g)$ and C generation. Neither is the case in heterogeneous catalysis. For ceria-based electrodes, their observed carbon tolerance during CO_2

electrolysis is loosely attributed to the enhanced oxygen-storage capacity [10]. Recent work showed that surface oxygen vacancies are saturated with carbonates during CO_2 electrolysis [27], which participates in the reduction of CO_2(g) to CO(g) on ceria [27–29]. However, the connection to carbon deposition, and more importantly, strategies to inhibiting it, remains elusive.

In this work, combining dense thin-film electrodes, *operando* ambient-pressure X-ray photoelectron spectroscopy (APXPS) and DFT calculations, we show that surface oxygen vacancies on ceria control the relative stability of carbonate (CO_2* on O, hereafter denoted as CO_2*_O, where the subscript indicates the bonding site), carboxylate ($CO*_O$) and adsorbed carbon monoxide ($C*_O$) reaction intermediates during CO_2 electrolysis, and therefore the onset overpotential for carbon deposition. Specifically, on the oxygen-vacancy-rich ceria surface, both experiments and computations show that carbon atoms are energetically trapped as oxidized carbon species relative to solid carbon (but not excessively trapped relative to CO(g)), thus delaying carbon formation. We propose that abundant carbonates on ceria, which are absent on Ni-YSZ, could also react and remove transiently deposited carbon to produce $CO*_O$ in a surface reverse-Boudouard reaction. Thus, two general design rules emerge: 1) To kinetically prevent carbon deposition during CO_2 electrolysis, carbon atoms need to be energetically trapped as oxidized carbon intermediates such that CO_2(g) and CO(g) are not easily reduced to carbon. 2) Having a high carbonate coverage facilitates the reverse Boudouard reaction. Finally, we use these insights to engineer and demonstrate a scaled-up 16 cm^2 SOC with a porous ceria electrode, achieving stable and selective CO_2 electrolysis beyond the thermodynamic carbon deposition threshold.

Operando X-ray photoelectron spectroscopy

To elucidate the carbon deposition mechanism on Ni and the carbon tolerance of ceria-based electrodes, *operando* APXPS [27,28,30,31] was carried out on three types of thin-film electrodes at 550 °C, schematically shown in Fig. 1: YSZ(100) single crystals with (Fig. 1a) dispersed Ni

nanoparticles and a microfabricated Ni patterned current collector ("Ni-YSZ"), (Fig. 1b) a samarium-doped ceria thin-film electrode grown by pulsed-laser deposition (PLD) with dispersed Ni nanoparticles and a buried patterned current collector ("Ni-SDC"), and (Fig. 1c) a Ni-free samarium-doped ceria thin-film electrode, also prepared by PLD and with a buried current collector ("SDC") [32]. These model electrodes represent the most common material sets employed in SOCs [7–10,14–17,22,33]. The counter electrode was nanoporous ceria/Pt for all samples. The gas atmosphere during APXPS measurements was chosen to avoid thermochemical Boudouard carbon deposition at open-circuit: 1:1 CO(g):CO_2(g) atmosphere with a total pressure of 480-500 mTorr for the Ni-SDC and Ni-YSZ electrodes, and 150 mTorr for the SDC electrode. At this temperature and pressure, the carbon deposition threshold is ~98% ±1% CO(g) balanced by CO_2(g) (uncertainty due to pressure range), much higher than the 50% CO(g) supply. Therefore, carbon deposition, if any, must be driven electrochemically by applying cathodic overpotential on the working electrode beyond the global thermodynamic threshold for carbon deposition, which corresponds to –120 ±72 mV overpotential (see Supplementary Note 1 and Supplementary Figure 1).

By gradually changing the overpotential from anodic to cathodic, we quantify the onset potential of carbon deposition for each electrode with APXPS, which is sensitive to the sub-monolayer of deposited carbon, and investigate the evolution of C- and O-containing species. As shown in Fig. 1g-i, carbon growth is indicated by the photoemission peak at ~285 eV. Quantified peak area as a function of overpotential is shown in Fig. 1j-l. For the Ni-YSZ electrode, adventitious carbon was present before biasing, as we did not flow oxygen prior to the experiment due to susceptibility of Ni to oxidation. Neither the carbon peak nor the lattice oxygen feature in O 1s photoemission peak (~530.5 eV at open-circuit for Ni-YSZ) changed significantly between +200 mV (anodic) to –100 mV (cathodic), just below the carbon deposition threshold. Upon reaching –150 mV overpotential, the intensity of the carbon peak grew considerably and continued to do so at larger overpotentials. This onset overpotential is close to the global thermodynamic threshold for carbon deposition, –120 ±72 mV. A concomitant decrease in the YSZ lattice oxygen peak from O

1s at –150 mV (Supplementary Figure 2) further confirms carbon deposition, which covers the oxide surface. Based on these observations, we postulate that only adventitious carbon is present on the sample between +200 mV (anodic) to –100 mV (cathodic), while at –150 mV additional carbon is deposited on account of the overpotential. The ceria-containing electrodes required a significantly higher overpotential to observe the onset of carbon formation. For Ni-SDC, the threshold was between –250 mV and –300 mV; for SDC in the absence of Ni, even higher overpotential is required – between –300 mV and –600 mV, consistent with previous APXPS observations that carbon can form on dense thin-film ceria electrodes with sufficiently high overpotential [34,35]. Notably, for all three electrodes, carbon can be partially removed by applying anodic overpotentials (Fig. 1g-i and Supplementary Figure 3).

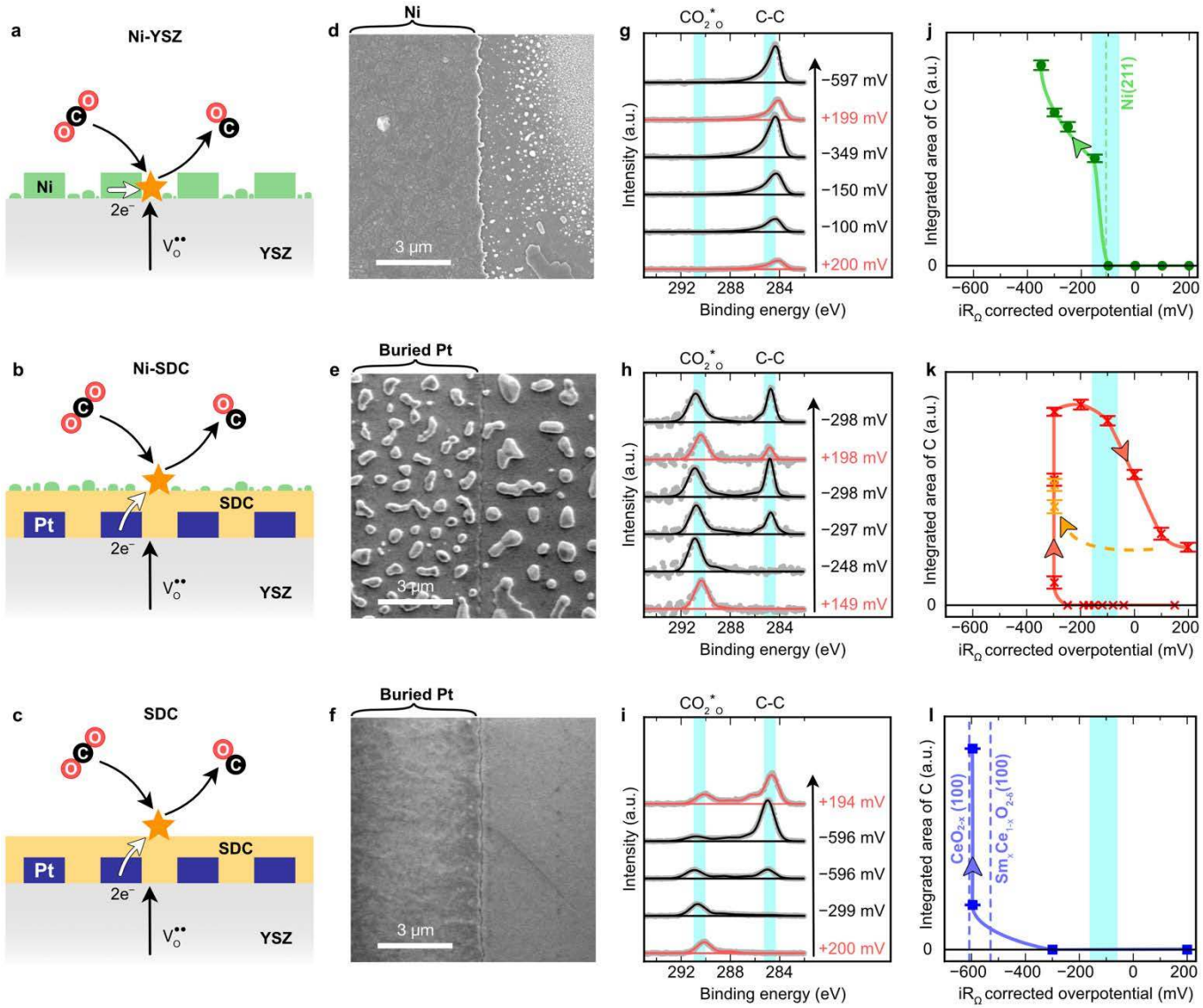

Fig. 1. Model electrodes employed and measurements of carbon formation/oxidation as the overpotential is varied. a-c, Illustrations of the Ni-YSZ, Ni-SDC, and SDC electrodes, with a buried Pt pattern for the SDC-containing electrodes. **d-f**, Planar SEM images of the surfaces and interfaces after testing. The Ni-YSZ electrode had <40 nm Ni particles next to the pattern. **g-i**, XPS spectra of C 1s with an inelastic mean free path of 0.6 nm showing the dependence of the carbon peak at ~285 eV on the applied overpotential (vs. $CO(g)/CO_2(g)/O^{2-}$, see Supplementary Note 1). The arrows indicate the chronological order of measurements. The blue shade indicates the binding energy range of $CO_2{}^*{}_O$ and C-C species. The binding energy of each spectrum at OCV are calibrated with the Au $4f_{7/2}$ peak (84.0 eV) from an Au foil Fermi coupled with the photoelectron analyzer. The gas phase peaks for CO and CO_2 have here been fitted and removed (Supplementary Figure 4), and all spectra have been normalized to the maximum carbon intensity. **j-l**, Integrated areas of the XPS C-C (~285 eV) peaks. Lines are only meant to guide the eye. Fitting error (standard deviation) is indicated by error bars. Adventitious carbon present on the Ni-YSZ sample

has been fitted and removed from **j**. The thermodynamic threshold for carbon formation is shown by the cyan bars, accounting for experimental uncertainties and differences. The dotted lines indicate the DFT calculated onset overpotentials, which will be discussed later.

As can be seen in the photoelectron spectra (Fig. 2a and also Fig. 1g-i), not only does the onset of carbon deposition vary dramatically between the three electrodes, but also the surface carbon chemistry. Across the electrode configurations and overpotentials examined, the C 1s spectra consist of asymmetric and/or multiple peaks, suggesting that a range of carbon-containing species form during electrolysis. See Supplemental Note 2 for fitting procedures. For Ni-YSZ, the binding energy (BE) shows mixed sp^2 and sp^3 type carbon (Fig. 2a, 284.3 and 284.7 eV, respectively [36–38]). The presence of sp^2 carbon, in particular, suggests the growth of graphitic carbon or carbon nanotubes, which indeed was observed by post mortem scanning electron microscopy (SEM) (Fig. 2b). On the other hand, for Ni-SDC and SDC electrodes, the summit BE is found close to 284.7 eV and peak fitting indicates that Ni-SDC (and SDC) electrodes deposit mostly sp^3 carbon, i.e., amorphous or diamond-like carbon [39]. No carbon with discernable microstructure was detected with post mortem SEM, consistent with carbon being deposited as a thin, amorphous layer. We note that because these carbon species are electronically (Fermi) coupled to the photoelectron analyzer, their BEs do not change with overpotential (as confirmed in Supplementary Figure 5), enabling a direct comparison to literature values. We also note that the quantification results are somewhat sensitive to the full-width half-maximum constraints applied. For completeness, we also investigated Ni carbide species through Ni 2*p* XPS for Ni-YSZ. The Ni $2p_{3/2}$ spectrum (Supplementary Figure 6) resembles that of a pure metal [40]. Thus, we conclude that there are no carbides, at least near the Ni surface.

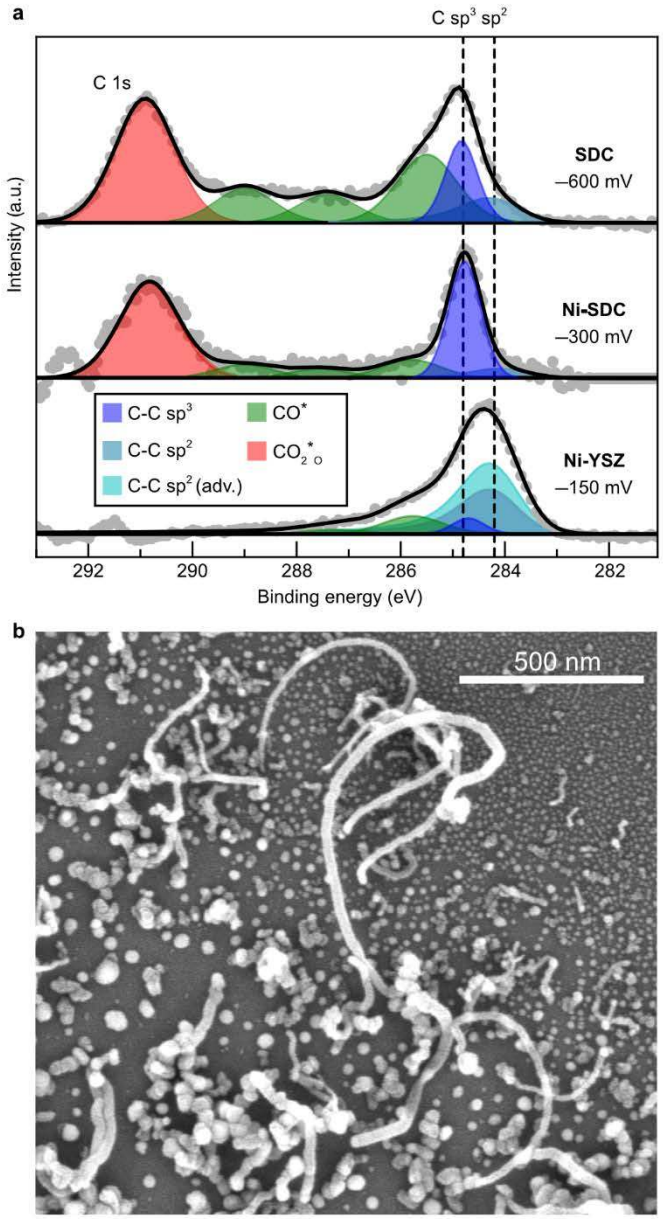

176

177 **Fig. 2. Surface carbon species observed with APXPS and SEM. a**, Fitting of XPS peaks for all
178 three electrodes at the electrode overpotential (rounded by 10 mV) where carbon was first
179 deposited. The gas phase peaks for CO and CO_2 have been fitted and removed (Supplementary
180 Figure 4), the background has been subtracted, and carbon peak intensity has been normalized. **b**,
181 Planar SEM of carbon nanotube growth on dispersed Ni nanoparticles next to the Ni pattern (Ni-
182 YSZ electrode). Scale bar is 500 nm.

183

184 The most pronounced spectroscopic difference between Ni-YSZ and the ceria-containing electrodes
185 is the presence of significant C 1s photoelectron intensities at BEs above that of the sp^2 and sp^3
186 carbon during CO_2 electrolysis, which correspond to various oxidized carbon species (Fig. 2a). The

fact that Ni-YSZ deposits carbon much more readily than Ni-SDC and SDC points to the importance of these oxidized carbon species. Specifically, on Ni-SDC and SDC electrodes, we observe significant amounts of carbonate (CO_2*$_O$) at all overpotentials (BE ~290.5 eV [27,31,41,42]) and various other oxygenated carbon species (CO*) such as C-O, C=O, and/or carboxylate (BE between ~ 286 and 290 eV, between the carbonate and carbon peaks [38,41–44]). As these peaks were not observed for Ni-YSZ and are qualitatively similar between Ni-SDC and SDC, we attribute them to species on ceria. It is noted that the BE shift of the CO_2*$_O$ peak with applied overpotential (Fig. 1h-i and Supplementary Figure 5) is likely due to CO_2*$_O$ not being Fermi coupled with the photoelectron analyzer [31], although a difference in adsorbate charge cannot be excluded.

Fig. 3 illustrates the evolution of these oxidized carbon species as a function of overpotential. For the ceria electrodes, carbonate adsorbate is present in high concentrations at all studied conditions. With increasing cathodic (reductive) overpotential prior to the onset of carbon deposition, the carbonate coverage grew, consistent with lattice oxygen near an oxygen vacancy being the adsorption site [27]. At the onset of carbon deposition, the carbonate coverage decreased significantly, likely corresponding to the coverage of the ceria surface with carbon and blockage of carbonate adsorption sites.

Next, we turn to other oxidized carbon species. These are generally less oxidized than carbonates, which we collectively refer to as CO*, as quantitative peak assignment is challenging. Before the onset of carbon deposition, their coverage is significantly lower than that of carbonates, approaching the detection limit. Interestingly, at the onset of carbon deposition, the signal for CO* increased concomitantly with carbon while the carbonate concentration decreased. We briefly speculate on the mechanism. Upon the formation of CO* adsorbate (carboxylate), two pathways are possible: (1) chemical desorption as CO(g) and (2) further electrochemical deoxygenation to C. These can occur in parallel. Before the onset of carbon deposition at around –300 mV, the first pathway prevails. Between –250 and –300 mV, the current density increases by 44%, which is accompanied by a significant increase in both carboxylate and carbon coverage. Given the large

jump in C and CO* coverage over a small voltage window and the lack of large change in current density, we associate the coverage change with electrochemical pathway (2) rather than chemical pathway (1). We first consider the possibility that the increase in CO* could be associated with the driving force needed to deposit C (i.e., buildup of reactant). This is possible if carbon deposition was the only reaction. An alternative explanation is that the buildup of CO* is due to the decomposition of C via the surface reverse Boudouard reaction, $2CO_2{}^*{}_O + C\text{-}C + 2S_O \rightarrow 4CO^*{}_O$, with S_O denoting an adsorbate-free oxygen site. If such a reaction proceeds quickly enough, it could establish a higher CO* coverage concomitant with increase in C coverage. This reaction occurs over the ceria surface for SDC, and additionally across the ceria/Ni/gas triple-phase boundary for Ni-SDC. The rate of this reaction is likely enhanced by the high carbonate coverage, which is a reactant. We note other pathways are also possible.

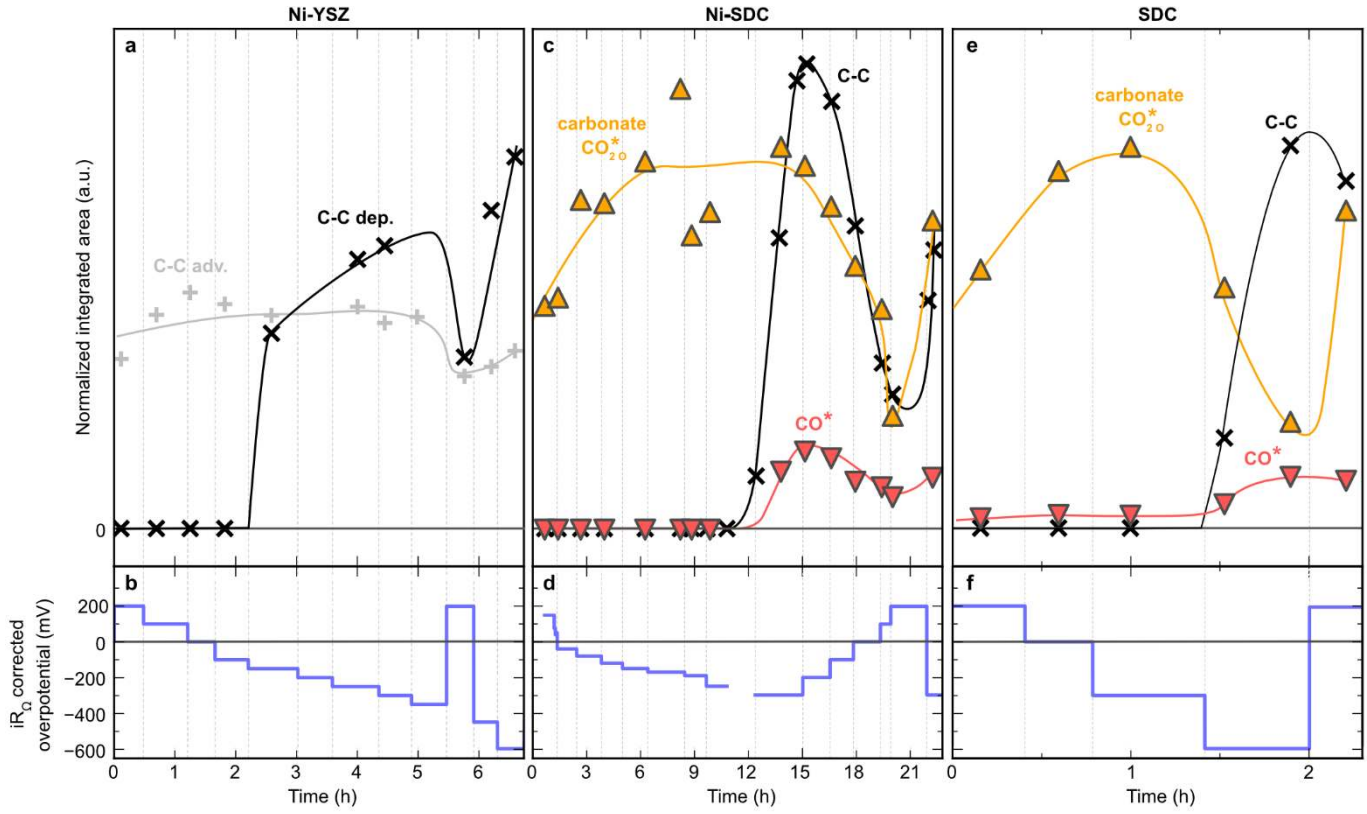

Fig. 3. Evolution of surface carbon species as overpotential is varied. a, **c** and **e**, Evolution of the normalized integrated areas of carbon, $CO_2{}^*{}_O$ and CO* from APXPS peaks with time for each electrode as the applied iR corrected overpotentials are varied, **b**, **d** and **f**. The integrated areas are averages of several measurements and were normalized to the CO_2(g) peak, which was normalized

to the absolute pressure. **a-b**, Ni-YSZ, **c-d**, Ni-SDC, and **e-f**, SDC. Lines are only meant to guide the eye. In **d**, voltage data was not recorded from ~11 to 12 h.

Density functional theory modeling

In order to shed light on the different behavior of the three electrodes, we modelled a series of (non)-stoichiometric ceria and Ni surfaces, and investigated the thermodynamics of various reaction intermediates by DFT. To use the same notation for Ni and ceria, we will now simplify the notation and omit the adsorption site as earlier indicated as subscript for CO_2*. We consider the adsorption of CO_2(g) and stepwise electrochemical deoxygenation, with each step being a two-electron process: $CO_{2(g)} \rightarrow CO_2^* \rightarrow CO^* + (O^{2-}{}_{YSZ} - 2e^-_{CC}) \rightarrow C^* + 2(O^{2-}{}_{YSZ} - 2e^-_{CC})$, where O^{2-} and e^- indicates the oxygen ions and electrons that migrate through the YSZ solid electrolyte and current collector (CC), respectively (Fig. 4). The overpotential is simulated via the Nernstian chemical potential of oxygen, $\Delta\mu O = \Delta\mu O^{2-}{}_{YSZ} - 2\Delta\mu e^-_{CC}$, where Δ indicates the difference with respect to open-circuit. The pathway starting with CO(g) is also implicitly calculated, but its chemical potential is fixed to CO_2(g) via $\Delta\mu O$ at zero energy. In the case of Ni, we do not explicitly simulate the three-phase boundary but rather include the electrochemical driving force via $\Delta\mu O$.

For ceria, we simulated bulk-truncated (111) stoichiometric CeO_2 and surface-only oxygen-deficient $CeO_{1.875}$ and $CeO_{1.75}$, as well as (100) and (110) surface-only oxygen-deficient $CeO_{1.875}$. Furthermore, we modelled a surface-only Sm-doped and oxygen-deficient $Sm_{0.25}Ce_{0.75}O_{1.875}$ (100), which is similar to the electrode characterized in the APXPS experiments (Fig. 4d). Given the YSZ substrate has a (100) termination, this is likely the termination of the SDC surface in our experiments, although we also considered (111) and (110) surfaces as these may coexist in the experiments. For oxygen-deficient ceria, which is experimentally relevant in the reducing atmosphere [27], DFT+U calculations reveal that (100) and (110) surfaces provide good anchoring sites for CO_2* adsorbates on oxygen, resulting in the formation of carbonate ($CO_2{}^*{}_O$) [45] with close to –2e charge (Supplementary Figure 7). The CO_2 adsorption Gibbs energy is the lowest for the

(100) surface (–0.9 eV at 550 °C), which is consistent with the high coverage measured spectroscopically. CO* species, on the other hand, adsorb on oxygen and are less sensitive to the surface termination. For both CO_2* and CO*, a ceria lattice oxygen is significantly displaced and participates in forming bridge-like carbonate and carboxylate adsorbates [46]. For $Sm_{0.25}Ce_{0.75}O_{1.875}$/$CeO_{1.875}$(100) and (110), O-vacancy also acts as the anchoring site for oxygen in CO_2* and CO* (Supplementary Figure 7). Finally, C* also adsorbs on the oxygen site forming typical CO-like species, while C* on the Ce site is considerably less stable by more than 4 eV. Fully oxidized CeO_2 are much less effective in stabilizing the carbonate, highlighting the importance of surface oxygen vacancies and/or Ce 4*f* localized electrons [27,42]. All species are stabilized by nearly identical amounts on the Sm-doped ceria $Sm_xCe_{1-x}O_{2-\delta}$ (100) surface, with Gibbs energies within 0.1 eV of $CeO_{2-\delta}$ (100) (see Supplementary Table 4 and Supplementary Figure 14). Considering additional variations – higher oxygen vacancy concentration, including the Ni(111) surface, or varying the CO_2(g)/CO(g) pressures – does not affect the conclusions drawn from the Gibbs energy calculations (Figs. S11-S14).

For Ni, we simulated the bulk-truncated (111) and (211) surfaces. We find that while CO_2(g) adsorbs on the stepped Ni(211) surface in a weakly bonded bent mode (Fig. 4c), the adsorption Gibbs energy is highly unfavorable (ΔG = 2.0 eV). In addition, Ni(211) has a higher affinity for carbon adsorption than Ni(111) (Figs. S11-S14) [47]. Because C* binds on Ni, it is significantly more stable than on ceria (on which it binds on O) by 1.0 to 2.0 eV (Fig. 4c).

Using the calculated adsorption Gibbs free energies, we determined the surface-specific thermodynamic overpotentials required for the electroreduction reactions from CO_2(g) and CO(g) to C to be downhill in energy. For $Sm_xCe_{1-x}O_{2-\delta}$ (100) and $CeO_{2-\delta}$ (100), this theoretical overpotential η is –530 and –610 mV, respectively, for the reduction of CO_2(g) to C and –504 and –460 mV, respectively, for the reduction of CO(g) to C. Both are significantly greater than the global thermodynamic overpotential for carbon deposition of –120 $\pm$72 mV, which is in good agreement with our experimental observations. We also find that η varies somewhat as a function of the

281 surface termination from –530 mV to –630 mV for the reduction of CO_2(g) to C on oxygen
282 deficient (111) and (110), respectively (Supplementary Table 3). Nonetheless, the theoretical values
283 are in good agreement with the experimental potentials between –300 mV and –600 mV obtained
284 via spectroscopic measurements (Fig. 1l). In contrast to ceria, for Ni(211), theoretical calculations
285 predict a η value of –110 mV for CO_2(g) or CO(g) reduction to C. We note that, because the CO_2*
286 adsorption Gibbs energy is very high on Ni, carbon deposition likely proceeds from CO(g).

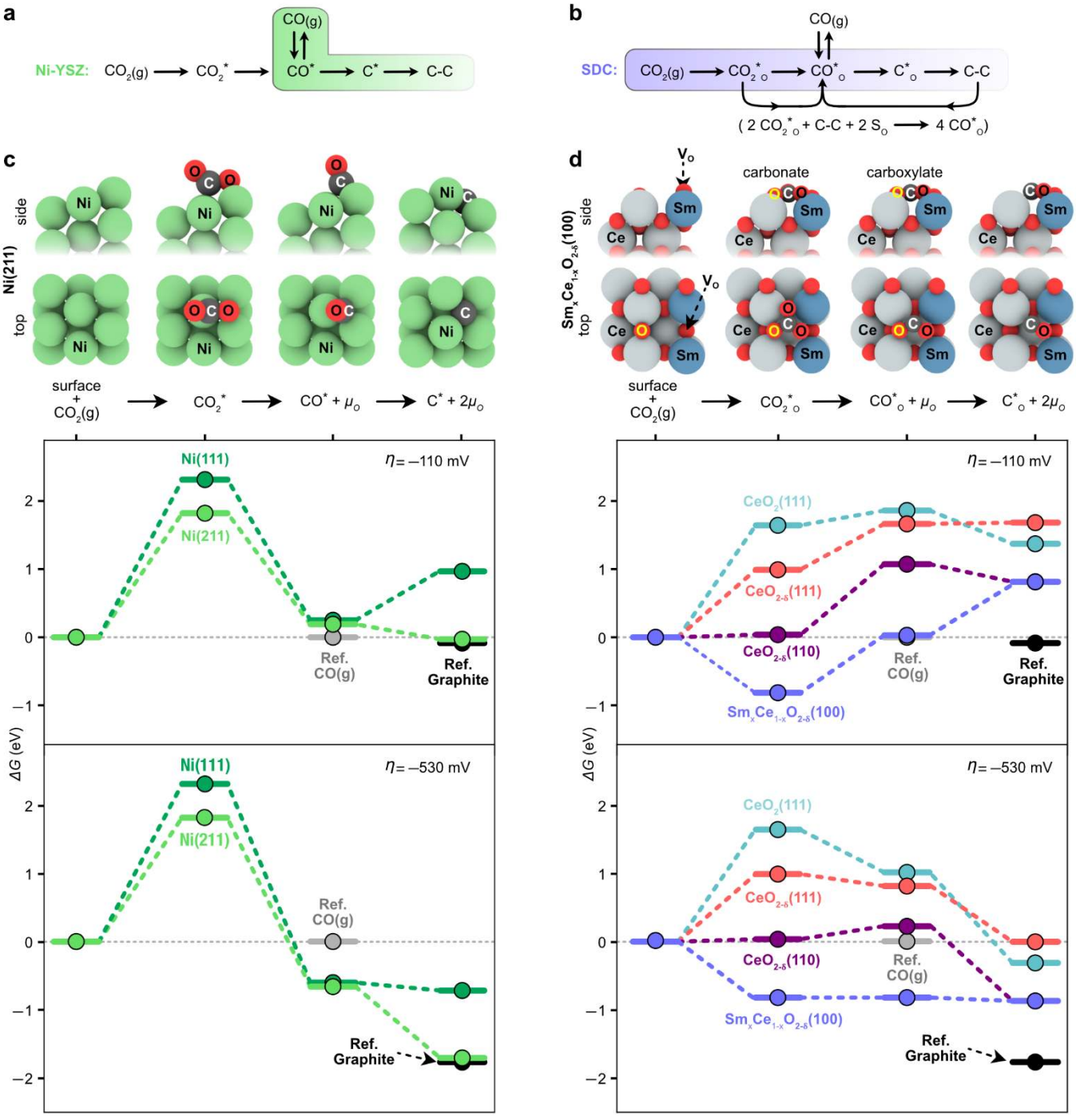

Fig. 4. Proposed reaction mechanism and calculated energetics for carbon formation on nickel and ceria surfaces. **a-b**, Reaction pathways for Ni-YSZ and SDC. **c-d**, Calculated free energy diagrams for Ni, $Sm_xCe_{1-x}O_{2-\delta}$ (100) and $CeO_{2-\delta}$ relative to the initial surfaces with gas-phase CO_2 and CO and oxidized carbon adsorbates under experimental conditions at overpotentials –110 mV and –530 mV. Structural evolution of the adsorbates on $Sm_xCe_{1-x}O_{2-\delta}$ (100) and Ni(211) surfaces is also shown, where the flat-laying carbonate species and bent CO_2 are stabilized via favorable oxygen bonding at the vacancy site. The yellow "O" labels on oxygen atoms indicate oxygen from

the ceria surface. Computational details and plots at other overpotential values are included in Supplementary Figures 8-9.

With these experimental and computational results at hand, the mechanism for ceria's carbon tolerance emerges. While the global reactions ($CO_2(g) \rightarrow C + 2(O^{2-}_{YSZ} - 2e^-_{CC})$ and $CO(g) \rightarrow C + (O^{2-}_{YSZ} - 2e^-_{CC})$) are downhill at overpotentials of –73 mV and –146 mV (see Supplementary Note 1 and Supplementary Figure 1), significant thermodynamic energy differences between CO_2*, CO* and C* at those potentials suppress the reaction. As shown in Fig. 4d for $Sm_xCe_{1-x}O_{2-\delta}$ (100) (blue trace), at –110 mV overpotential (near the global thermodynamic carbon deposition threshold), CO_2*_O (carbonate) is by far the most stable, followed by $CO*_O$ (~0.1 eV) and finally by $C*_O$ (~1.0 eV above graphite). Importantly, because the energy barriers are positive for the progressive reduction of the carbonate adsorbate, and $CO*_O$ has a negligible adsorption energy with respect to CO(g), selective CO_2(g) reduction to CO(g) is expected. On the other hand, in Fig. 4c, Ni(211) (green trace) exhibits precisely the opposite, with C* being the most stable. APXPS shows identical trends in terms of adsorbate coverage for ceria. Here, the carbonate and CO* trap the carbon, enabled by the large free energy difference between carbonate, CO* and C* and hinders the reaction to proceed to the global equilibrium. Applying a cathodic overpotential of –530 mV flattens the energy landscape such that the traps disappear (Fig. 4d blue trace), again consistent with our observation that carbon eventually deposits at large overpotentials. The large CO_2* adsorption energy is also crucial, as it establishes a high carbonate coverage (observed also in APXPS) and could provide a driving force for the surface reverse-Boudouard reaction (ΔG_{rxn} = 0.31 eV for $CeO_{1.875}$(100)) to remove transiently deposited carbon (Fig. 4b). Thus, the two key requirements for suppressing carbon deposition satisfied by $CeO_{1.875}$(100) are: (1) trapping carbon in oxidized carbon intermediates, and (2) establishing a high carbonate coverage. We predict that (100) and (110) surface terminations best satisfy these requirements (Fig. 4d). Higher oxygen deficiency increases

this effect (Supplementary Figure 16). Hence, dependence on surface termination and oxygen vacancy concentration highlight the tunability of carbon suppression.

Technological demonstration with scaled-up cells

With these insights, we demonstrated technological feasibility by fabricating 16 cm^2 SOCs with nanostructured, porous Gd-doped ceria negative-electrodes and testing the carbon-tolerance of these scaled-up cells during CO_2 electrolysis operation at 750 °C (Fig. 5). For comparison, we also tested a state-of-the-art Ni-YSZ based cell in approximately identical conditions, for comparison [9]. Similar to the model electrodes, we increased the electrolysis current density stepwise until the cell voltage began to rapidly increase, indicating carbon deposition. The cell with Ni-YSZ electrode showed carbon deposition at an outlet CO partial pressure of ~73%, lower than the thermodynamic Boudouard threshold (78% CO, balance CO_2) [9,13] (Fig. 5a). As in the case of the model ceria electrode, the cell with porous ceria electrode was able to operate past the threshold. We proceeded to carry out CO_2 electrolysis to produce CO beyond the threshold for more than 10 h with stable cell voltage (Fig. 5b). We then probed the operating limit, which we found to be ~95% CO at the outlet (Fig. 5a), and we could subsequently recover performance by oxidizing the deposited carbon. Post-mortem SEM images showed a damaged Ni-YSZ electrode (delamination between electrode and electrolyte) and an intact ceria electrode (Fig. 5c). Considering also electrochemical carbon deposition rather than only Boudouard deposition, the driving force is even further past the threshold (Supplementary Figure 10).

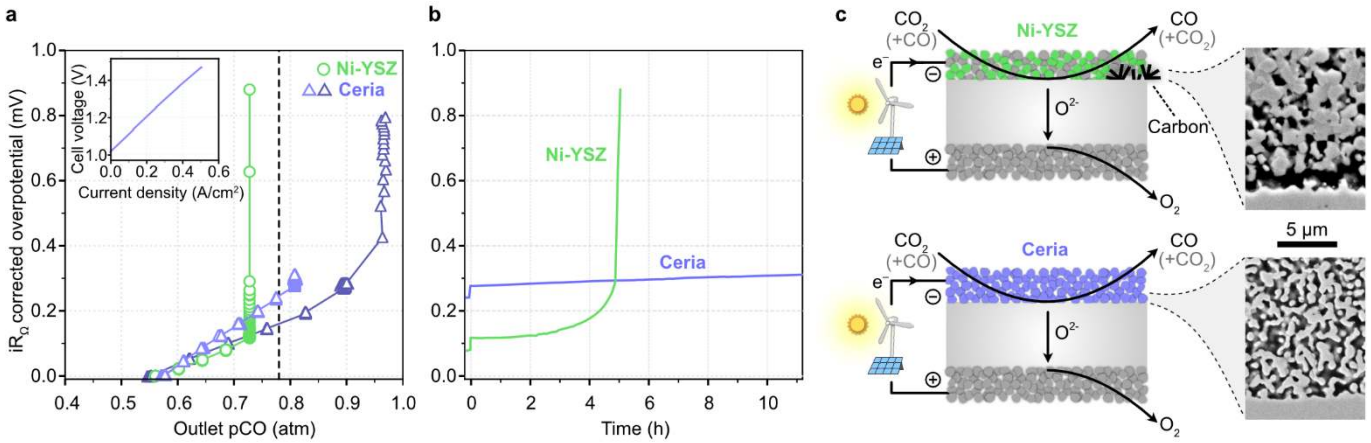

Fig. 5. Comparison of the abilities of scaled-up solid oxide cells with Ni-YSZ vs ceria electrodes to suppress carbon deposition during CO_2 electrolysis. a, Measured outlet CO partial pressure (balance CO_2) and cell overpotential corrected for ohmic potential drop (iR_Ω, where R_Ω is the ohmic area-specific resistance) at increasing applied current densities. The dashed vertical line is the thermodynamic threshold of carbon deposition via the Boudouard reaction. Inset: Typical electrolysis current-voltage curve measured on a cell with ceria negative-electrode. **b**, Part of the same data in **a**, now shown as a function of time at two of the final operating points (fixed current density, 0.35 A/cm^2 for the ceria cell and 0.5 A/cm^2 for the Ni-YSZ cell). **c**, Illustrations of the two cell types and post-test cross-sectional SEMs at the gas outlet near the negative-electrode/electrolyte interfaces where carbon deposited in the Ni-YSZ electrode and caused interface delamination. The cells had 16 cm^2 active area and were operated at 750 °C and 1 atm pressure in a plug-flow test configuration. Further test information is given in Methods and Supplementary Figure 10.

Conclusions

The remarkable carbon-suppression capability of ceria, now rationalized in this work, has major implications for stable and selective CO_2 electrolysis. First, it offers robustness against a hard-failure mode that can immediately end device lifetime. Electrolysis on ceria electrodes may still be carried out in safe conditions, now with the insurance that the electrolyzer can survive operational accidents. Eliminating the risk of cell death could have major impact on commercial CO and fuel production device economics and could be especially beneficial for mission-critical applications, such as solid oxide CO_2 electrolyzers that will be used on Mars (to be first demonstrated on NASA's 2020 rover mission). Second, it is possible to push operation into

conventionally unsafe conditions and thereby obtain higher yields of fuel and O_2 product. The ability to achieve a higher CO concentration, which is limited to well below 50% in today's cell stacks due to thermodynamics and gradients [9], would reduce the cost of downstream separation to obtain a pure CO product.

The next step towards full-scale CO_2 electrolysis technology is integration of these nickel-free, nanostructured ceria electrodes into alternative cell designs that provide improved electronic current collection and lower overall cell resistance than the electrolyte-supported cells used in this demonstration. Metal-supported or oxygen-electrode-supported cells with thin electrolytes are candidates that do not rely on nickel for structural support and current collection, unlike the majority of cells being developed.

Finally, the new mechanistic understanding gained from our *operando* spectroscopy experiments and DFT modeling will guide the tuning of the surface properties of ceria and other vacancy-rich oxides to further improve carbon-tolerance. More generally, our insights and approach could contribute to achieving stable and selective catalytic reactions involving carbon chemistry.

Methods

Preparation of Model Electrode Cells

The single-chamber model electrochemical cells were fabricated on single-crystal (100) $Y_{0.16}Zr_{0.84}O_{1.92}$ (YSZ) substrates acting as the oxygen-ion-conducting electrolyte with dimensions 10 x 10 x 0.5 mm^3, with one side polished. The fabrication procedure follows in chronological order. The counter-electrode (CE) was applied on the rough side of the substrate by hand-painting Pt paste (Ferro GmbH 64021015), which was dried on a hot-plate at 200 °C and sintered at 800 °C for 1 h in stagnant air, forming a porous Pt backbone. Next, an aqueous precursor salt solution for Pr-doped ceria (PDC) [33] was wet infiltrated, dried at 250 °C on a hot-plate and decomposed at 350 °C for 0.5 h in stagnant air. The PDC was introduced to enhance the oxygen-ion-conducting and electrocatalytic

capabilities. The large area and relatively high performance of the CE ensured that the prevalent part of the potential-drop was across the working-electrode (WE), with a minor (<1 %) drop over the electrolyte. The exact overpotential of the CE was not determined, but assumed to be insignificant. The overpotential of the WE was thus estimated as $\eta_{WE} = V_{cell} - I_{cell}R_{\Omega}$, with R_{Ω} found by electrochemical impedance spectroscopy (EIS). On the polished side, the Pt or Ni current conducting pattern was fabricated by metal lift-off photolithography. An undercut resist layer (Dow Microposit LOL 2000) was spin-coated on the polished side of the YSZ substrate at 2000 r.p.m. for 60 s (~300nm thick) and annealed in air at 180 °C for 5 minutes. To the annealed undercut layer, a positive photoresist (Shipley S-1813) was spin-coated at 4000 r.p.m. for 45 s and baked at 100 °C for 2.5 min underneath a glass cover. The photomask was aligned with a Karl Suss MJB 3 mask aligner and the spin-coated films were exposed to UV light with a dosage of 105 mJ. The photoresist was developed in a Shipley Microposit MF CD-26 Developer solution until the undercut was ~1 μm. After the pattern was rinsed with deionized water, dried, oxygen plasma cleaned for 30 secs at 200 W, the metal was deposited in 2250 mTorr Ar in a DC magnetron Lesker sputter system. Liftoff was accomplished dissolving the resist in Baker PRS-1000 Positive Photoresist stripper heated to 50 °C. A final oxygen plasma treat at 300 W for 60s ensured removal of any photolithographic residue. The Pt pattern current collector consisted of 27 x 2000 µm stripes of 180 nm height and 5 µm width separated by 10 µm. A closed loop design improved interconnectivity to prevent disconnected metal stripes due to defects in the photolithography process; 500 x 750 μm^2 Pt contact pads were placed on the side of the patterns for contact with the current collector probe (Supplementary Figure 11). The Ni pattern consisted of 13 x 2000 µm stripes of 200 nm height and 5 µm width separated by 50 µm. A closed loop design was used again to ensure metal connectivity. A 500 x 750 μm^2 Ni contact pad was placed at one end of the pattern for probe contact. Each YSZ patterned sample had two WEs so that the biased electrode could be compared to a reference sample exposed to identical experimental conditions but left unbiased. The Pt was annealed at 650 °C for 1 h in 100 mTorr, On the Pt pattern samples, a 650 µm thick $Sm_{0.2}Ce_{0.8}O_{1.9-\delta}$ (SDC) film was deposited by pulsed-laser deposition at 650

°C in 5 mTorr O_2 with a laser fluency of 1.5 J cm^{2-} at 10 Hz with a substrate to target distance of 70 cm. For the Ni-SDC sample, an additional 35 nm thick NiO layer was deposited by PLD on top of the SDC. The NiO layer was reduced to randomly dispersed, approximately 200-400 nm, Ni particles in-situ during the XPS experiment with a 500 mTorr CO:CO_2 (1:1) atmosphere. The Ni-YSZ sample had Ni particles next to the Ni pattern, which varied in size from 40 nm to less than 1 nm.

Electrochemical XPS

Ambient-pressure XPS experiments were conducted at beamline 9.3.2 [48] (Ni-SDC and SDC samples) and beamline 11.0.2 [49] (Ni-YSZ sample) at the Advanced Light Source synchrotron, Lawrence Berkeley National Laboratory. Scienta R4000 HiPP and Specs Phoibos 150 differentially pumped electron analyzers are employed for beamline 9.3.2 and 11.0.2, respectively, which together with a homebuilt sample holder (Supplementary Figure 11) allows for experimental conditions of up to 700 °C [50] and 1000 mTorr [48], or several thousand mTorr for 11.0.2. Ohmic heating was supplied by a ceramic heater. Electrical contact was established by mechanically pressing a Pt coil onto the CE, while the electrical contact to the WE was made by Pt/Ir probes. More details on the design of the sample holder can be found elsewhere [49,50].

A similar kinetic energy was applied, when possible, namely 160 – 320 eV. Incident angle from the sample normal was 75 ° for the SDC and Ni-SDC samples at beamline 9.3.2, while it was 65 ° for Ni-YSZ at beamline 11.0.2. This and other differences between the two beam-lines, such as width of incident beam and distance between sample and the aperture, causes significantly different gas phase peak intensity between the samples, and a slightly different gas phase BE as seen in Supplementary Figure 4. This did however not affect the data analysis significantly. The WE and an Au foil were Fermi coupled with the electron analyzer. The BE of each spectrum at OCV was calibrated with the Au $4f_{7/2}$ peak (84.0 eV). A Biologic SP-300 potentiostat was used for chrono-amperometry and EIS. The latter was used to estimate the temperature by comparing the ohmic resistance, R_Ω, to that

441 measured during a calibration experiment. R_Ω of a similar sample on the same sample holder was
442 measured in a tube furnace in 500 mTorr O_2 and correlated to the temperature measured with a
443 thermocouple. The thermal conductivity of O_2 is similar to that of CO and CO_2, but the different gas
444 atmosphere does introduce some uncertainty. A change in total pressure from 500 mTorr to 50 mTorr,
445 which far exceeds the uncertainty during the experiments, correspond to a temperature uncertainty of
446 $\pm$7 °C. During the experiments at 550 °C, the heater was used to adjust R_Ω with an accuracy of $\pm$100
447 Ω, which translates to an additional uncertainty of $\pm$3 °C. Thus, a total uncertainty in temperature
448 measurements is estimated to no more than $\pm$10 °C.

449 During the experiments, adventitious carbon was first burned off for the SDC and NiO-SDC samples
450 by flowing O_2 at 550 °C. This was not possible for the Ni-YSZ sample, as the metallic Ni pattern
451 would undergo a redox cycle to NiO potentially causing an electrical disconnection of part of the
452 electrode. CO and CO_2 of research grade purity was then carefully dosed and equilibrated to a ~1:1
453 ratio, which was confirmed by means of the XPS gas phase peaks intensities calibrated for the
454 difference in electron-molecule scattering cross-sections of CO and CO_2 [51], as well as with a residual
455 gas analyzer.

456

457 Density Functional Theory

458 DFT calculations were performed within the Hubbard-U method (DFT+U) using the Vienna Ab initio
459 Simulation Package (VASP, version 5.4.1) using the nearly identical settings as in our recent paper
460 on CeO_2 [52]. The use of PAW potentials, 500 eV plane-wave cutoff, U_{eff}(Ce, Sm) = 4.5 eV [53,54] and
461 dense (9x9x9) k-point grid resulted in the equilibrium lattice parameter of a = 5.497 Å for CeO_2 and
462 a = 3.52 Å for Ni . Our simulation cells for ceria surfaces contained a minimum of 3 layers (and 4 for
463 Ni surfaces) with a 2x2 (3x2) periodicity. The two topmost layers were always allowed to relax until
464 the forces were lower than 0.02 eV A^{-1} using a 5x5x1 k-point mesh.

In the CeO_2 DFT calculations, the top-only surface oxygen vacancy concentration [V_O] is held fixed at zero for "CeO_2 (111)", at 25% for "$CeO_{2-\delta}$ (1xx)" (x being 0 or 1) or "$CeO_{2-\delta}$ (1xx)|25% V_O", or at 50% for "$CeO_{2-\delta}$ (111)|50% V_O" in Supplementary Figures 7-9 and Supplementary Figures 14-18, and [V_O] is not affected by applied overpotential. In reality, CO_2* and [V_O] vary with overpotential [27].

Because of the elevated temperature nature of CO_2 electrolysis in SOCs (823 K in this work), we include vibrational entropy as well as configurational entropy of gas molecules, which affects the calculated free energies significantly relative to T = 0 K enthalpy values, Supplementary Tables 4 and 5. Using these calculated adsorption energies, we determined the overpotentials required for the electrochemical reduction reactions from CO_2(g) and CO(g) to C, defined as the potential at which the C* becomes exergonic with respect to the previous reaction steps. When a cathodic overpotential is applied, CO* free energy is shifted down by $2e\eta$ and C* by $4e\eta$, where η is the theoretical overpotential. We rationalize using a thermodynamic approach because reasonable kinetic rates (~1 $site^{-1}s^{-1}$) are expected for barriers as large as 2 eV at the operating temperature of 800 K [55].

Scaled-up cells

Two cells of different type with 16 cm^2 active area were tested: one nickel-electrode reference cell and one carbon-tolerant ceria-electrode cell. Both cells were tested in a plug-flow set-up [56] with pO_2 sensors just upstream and downstream of the cell, placed into the fuel-side gas flow. These pO_2 values were used, together with leak analysis, to quantify the outlet pCO. Absolute or positive pO_2 voltage values are used throughout; 1000 mV corresponds to a very small quantity of oxygen such as 10^{-20} atm. Photos of the experimental setup can be seen in Supplementary Fiure. 11.

The reference cell was a state-of-the-art porous Ni-YSZ supported cell produced by Haldor Topsoe A/S. The dense ~10 µm thick electrolyte consisted of 8 mol% Y-doped zirconia (8YSZ) and a Gd-doped ceria (GDC) barrier layer, and the porous oxygen electrode was a composite of GDC and lanthanum-strontium-cobalt-ferrite. The Ni-3YSZ support was ~300 µm thick with a 10-30 µm active

Ni-8YSZ electrode layer. The fuel gas compartment was sealed with gold to an alumina test house, and nickel and gold meshes functioned as current collectors and gas distributors for the fuel and oxygen side, respectively. After reduction of NiO to Ni at 850 °C and initial performance characterization, the cell was tested with 14 L/h CO and 9 L/h CO_2, and a current density of 0.5 A/cm^2. Further details about this cell can be found in ref. [9].

The cell with enhanced carbon tolerance was a 150 µm thick dense 10Sc1CeSZ electrolyte-supported cell with a 35-50 µm thick porous GDC backbone sprayed on both sides (10Sc1CeSZ is ZrO_2 doped with 10 mol% Sc_2O_3 and 1 mol% CeO_2). The oxygen side was infiltrated with 3 cycles of an aqueous solution comprising 1.63 M metal nitrates corresponding to $La_{0.75}Sr_{0.25}MnO_3$. The cell was heated to 1000 °C to form that perovskite phase on the GDC backbone. The oxygen side was then infiltrated with 1 cycle of 3 M Ce and Pr nitrates solution with Ce:Pr 8:2 ratio (for forming PDC upon heating), and the fuel side was infiltrated with 1 cycle of a 3 M Ce and Gd nitrates solution with Ce:Gd 8:2 ratio, to enhance the electrochemical performance. The infiltration solutions were prepared from the respective metal nitrates mixed in DI water with a Triton X-100 surfactant. Pt-paste was used as a current-collection layer on both sides of the cell (Supplementary Figure 11). The cell was mounted in a similar manner as the Ni-YSZ cell, but with a Pt mesh as the current collector and gas distributor on the fuel side (Supplementary Figure 11). The cell was tested multiple times beyond the carbon deposition onset threshold. The gas flow used for Fig. 5 without carbon deposition was 7 L/h of CO and 4.5 L/h of CO_2 to the fuel side, and 40 L/h of O_2 to the oxygen side. The applied current density was 0.35 A/cm^2. The measured pO_2 of the outlet gas was 1031 mV, above the carbon deposition threshold of 1024 mV at the 750 °C operating temperature. For the test that showed cell voltage increase due to carbon deposition, the flow rates were 3.5 L/h CO and 2.25 L/h CO_2, with a current density of 0.3 A/cm^2. Including a minor cross-over leak, the resulting inlet gas at the cell had a pCO_2 of 40-45% (Fig. 5). The measured pO_2 of the outlet gas reached 1114 mV before the test was stopped. Prior CO_2 electrolysis works report testing with inlet pCO_2 ranging from 10% to 100% [1,5,8–10,13]. In a commercial system, a pCO_2 closer to 100% may be preferable and more realistic, however for nickel-

containing electrodes the pCO_2 of the supplied gas must not be too close to 100% to avoid oxidation of the nickel. The test conditions here were chosen based on recent detailed high-temperature CO_2 electrolysis studies [9,13] to minimize concentration gradients and overpotentials and to begin (at open-circuit condition) relatively close to the thermodynamic carbon deposition threshold (pCO_2 of 22%), ensuring that carbon deposition conditions could be reached without inducing other known degradation mechanisms that are driven by large gradients and overpotentials [7,9,13].

Data Availability

Data underlying the study can be found at Figshare[57] (APXPS and cell testing) and https://www.catalysis-hub.org/publications/SkafteSelective2019 (DFT)[58].

References:

1. Jensen, S. H., Larsen, P. H. & Mogensen, M. Hydrogen and synthetic fuel production from renewable energy sources. *Int. J. Hydrogen Energy* **32,** 3253–3257 (2007).
2. Graves, C., Ebbesen, S. D., Mogensen, M. & Lackner, K. S. Sustainable hydrocarbon fuels by recycling CO_2 and H_2O with renewable or nuclear energy. *Renew. Sustain. Energy Rev.* **15,** 1–23 (2011).
3. Seh, Z. W. *et al.* Combining theory and experiment in electrocatalysis: Insights into materials design. *Science* **355,** eaad4998 (2017).
4. Davis, S. J. *et al.* Net-zero emissions energy systems. *Science* **360,** eaas9793 (2018).
5. Bidrawn, F. *et al.* Efficient Reduction of CO_2 in a Solid Oxide Electrolyzer. *Electrochem. Solid-State Lett.* **11,** B167 (2008).
6. Jensen, S. H. *et al.* Large-scale electricity storage utilizing reversible solid oxide cells combined with underground storage of CO_2 and CH_4. *Energy Environ. Sci.* **8**, 2471-2479

(2015).

7. Graves, C., Ebbesen, S. D., Jensen, S. H., Simonsen, S. B. & Mogensen, M. B. Eliminating degradation in solid oxide electrochemical cells by reversible operation. *Nat. Mater.* **14,** 239–244 (2015).

8. Hartvigsen, J., Elangovan, S., Elwell, J. & Larse, D. Oxygen Production from Mars Atmosphere Carbon Dioxide Using Solid Oxide Electrolysis. *ECS Trans.* **78,** 2953–2963 (2017).

9. Skafte, T. L., Blennow, P., Hjelm, J. & Graves, C. Carbon deposition and sulfur poisoning during CO_2 electrolysis in nickel-based solid oxide cell electrodes. *J. Power Sources* **373,** 54–60 (2018).

10. Duboviks, V. *et al.* A Raman spectroscopic study of the carbon deposition mechanism on Ni/CGO electrodes during CO/CO_2 electrolysis. *Phys. Chem. Chem. Phys.* **16,** 13063 (2014).

11. Helveg, S. *et al.* Atomic-scale imaging of carbon nanofibre growth. *Nature* **427,** 426–429 (2004).

12. Tao, Y., Ebbesen, S. D. & Mogensen, M. B. Carbon Deposition in Solid Oxide Cells during Co-Electrolysis of H_2O and CO_2. *J. Electrochem. Soc.* **161,** F337–F343 (2014).

13. Navasa, M., Frandsen, H. L., Skafte, T. L., Sundén, B. & Graves, C. Localized carbon deposition in solid oxide electrolysis cells studied by multiphysics modeling. *J. Power Sources* **394,** 102–113 (2018).

14. Homel, M., Gür, T. M., Koh, J. H. & Virkar, A. V. Carbon monoxide-fueled solid oxide fuel cell. *J. Power Sources* **195,** 6367–6372 (2010).

15. Boldrin, P. *et al.* Strategies for Carbon and Sulfur Tolerant Solid Oxide Fuel Cell Materials, Incorporating Lessons from Heterogeneous Catalysis. *Chem. Rev.* **116,** 13633–13684 (2016).

16. Murray, E. P., Tsai, T. & Barnett, S. A. A direct-methane fuel cell with a ceria-based anode.

564 *Nature* **400,** 649–651 (1999).

565 17. Park, S., Vohs, J. M. & Gorte, R. J. Direct oxidation of hydrocarbons in a solid-oxide fuel
566 cell. *Nature* **404,** 265–267 (2000).

567 18. Yang, L. *et al.* Enhanced Sulfur and Coking Tolerance of a Mixed Ion Conductor for SOFCs:
568 $BaZr_{0.1}Ce_{0.7}Y_{0.2-x}Yb_xO_{3-\delta}$. *Science* **326,** 126–129 (2009).

569 19. Li, X. *et al.* In Situ Probing of the Mechanisms of Coking Resistance on Catalyst-Modified
570 Anodes for Solid Oxide Fuel Cells. *Chem. Mater.* **27,** 822–828 (2015).

571 20. Choi, Y., Brown, E. C., Haile, S. M. & Jung, W. Electrochemically modified, robust solid
572 oxide fuel cell anode for direct-hydrocarbon utilization. *Nano Energy* **23,** 161–171 (2016).

573 21. Skafte, T. L., Sudireddy, B. R., Blennow, P. & Graves, C. Carbon and Redox Tolerant
574 Infiltrated Oxide Fuel-Electrodes for Solid Oxide Cells. *ECS Trans.* **72,** 201–214 (2016).

575 22. Irvine, J. T. S. *et al.* Evolution of the electrochemical interface in high-temperature fuel cells
576 and electrolysers. *Nat. Energy* **1,** 15014 (2016).

577 23. Rostrup-Nielsen, J. R. & Alstrup, I. Innovation and science in the process industry: Steam
578 reforming and hydrogenolysis. *Catal. today* **53,** 311–316 (1999).

579 24. Mortensen, P. M. & Dybkjær, I. Industrial scale experience on steam reforming of CO_2-rich
580 gas. *Appl. Catal. A Gen.* **495,** 141–151 (2015).

581 25. Guo, J. *et al.* Improving the Carbon Resistance of Ni-Based Steam Reforming Catalyst by
582 Alloying with Rh: A Computational Study Coupled with Reforming Experiments and
583 EXAFS Characterization. *ACS Catal.* **1,** 574–582 (2011).

584 26. Nikolla, E., Schwank, J. & Linic, S. Hydrocarbon steam reforming on Ni alloys at solid
585 oxide fuel cell operating conditions. *Catal. Today* **136,** 243–248 (2008).

586 27. Feng, Z. a., Machala, M. L. & Chueh, W. C. Surface electrochemistry of CO_2 reduction and
587 CO oxidation on Sm-doped CeO_{2-x}: coupling between Ce^{3+} and carbonate adsorbates. *Phys.*

588 *Chem. Chem. Phys.* **17,** 12273–12281 (2015).

589 28. Yu, Y. *et al.* CO_2 activation and carbonate intermediates: an operando AP-XPS study of CO_2
590 electrolysis reactions on solid oxide electrochemical cells. *Phys. Chem. Chem. Phys.* **16,**
591 11633–11639 (2014).

592 29. Cheng, Z., Sherman, B. J. & Lo, C. S. Carbon dioxide activation and dissociation on ceria
593 (110): A density functional theory study. *J. Chem. Phys.* **138,** 1–20 (2013).

594 30. Zhang, C. *et al.* Measuring fundamental properties in operating solid oxide electrochemical
595 cells by using in situ X-ray photoelectron spectroscopy. *Nat. Mater.* **9,** 944–949 (2010).

596 31. Opitz, A. K. *et al.* Surface Chemistry of Perovskite-Type Electrodes During High
597 Temperature CO_2 Electrolysis Investigated by Operando Photoelectron Spectroscopy. *ACS*
598 *Appl. Mater. Interfaces* **9,** 35847–35860 (2017).

599 32. Chueh, W. C., Hao, Y., Jung, W. & Haile, S. M. High electrochemical activity of the oxide
600 phase in model ceria–Pt and ceria–Ni composite anodes. *Nat. Mater.* **11,** 155–161 (2012).

601 33. Graves, C., Martinez, L. & Sudireddy, B. R. High Performance Nano-Ceria Electrodes for
602 Solid Oxide Cells. *ECS Trans.* **72,** 183–192 (2016).

603 34. Yu, Y. *et al.* Carbon Deposits and Pt/YSZ Overpotentials in CO/CO_2 Solid Oxide
604 Electrochemical Cells. *ECS Trans.* **57,** 3119–3126 (2013).

605 35. Wang, J. *et al.* Threshold catalytic onset of carbon formation on CeO_2 during CO_2
606 electrolysis: Mechanism and inhibition. *J. Mater. Chem. A* **7**, 15233–15243 (2019).

607 36. Morar, J. F. *et al.* C 1s excitation studies of diamond (111). I. Surface core levels. *Phys. Rev.*
608 *B* **33,** 1346–1349 (1986).

609 37. Haerle, R., Riedo, E., Pasquarello, A. & Baldereschi, A. sp^2/sp^3 hybridization ratio in
610 amorphous carbon from C 1s core-level shifts: X-ray photoelectron spectroscopy and first-
611 principles calculation. *Phys. Rev. B* **65,** 045101 (2001).

612 38. Ermolieff, A. *et al.* XPS, Raman spectroscopy, X-ray diffraction, specular X-ray reflectivity,
613 transmission electron microscopy and elastic recoil detection analysis of emissive carbon
614 film characterization. *Surf. Interface Anal.* **31,** 185–190 (2001).

615 39. Alzate-Restrepo, V. & Hill, J. M. Carbon deposition on Ni/YSZ anodes exposed to CO/H_2
616 feeds. *J. Power Sources* **195,** 1344–1351 (2010).

617 40. El Gabaly, F., McCarty, K. F., Bluhm, H. & McDaniel, A. H. Oxidation stages of Ni
618 electrodes in solid oxide fuel cell environments. *Phys. Chem. Chem. Phys.* **15,** 8334 (2013).

619 41. Mudiyanselage, K. *et al.* Importance of the Metal-Oxide Interface in Catalysis: In Situ
620 Studies of the Water-Gas Shift Reaction by Ambient-Pressure X-ray Photoelectron
621 Spectroscopy. *Angew. Chemie - Int. Ed.* **52,** 5101–5105 (2013).

622 42. Staudt, T. *et al.* Electronic Structure of Magnesia-Ceria Model Catalysts, CO_2 Adsorption,
623 and CO_2 Activation: A Synchrotron Radiation Photoelectron Spectroscopy Study. *J. Phys.*
624 *Chem. C* **115,** 8716–8724 (2011).

625 43. Czekaj, I. *et al.* Characterization of surface processes at the Ni-based catalyst during the
626 methanation of biomass-derived synthesis gas: X-ray photoelectron spectroscopy (XPS).
627 *Appl. Catal. A Gen.* **329,** 68–78 (2007).

628 44. Ming, H. *et al.* Large scale electrochemical synthesis of high quality carbon nanodots and
629 their photocatalytic property. *Dalt. Trans.* **41,** 9526 (2012).

630 45. Paier, J., Penschke, C. & Sauer, J. Oxygen Defects and Surface Chemistry of Ceria: Quantum
631 Chemical Studies Compared to Experiment. *Chem. Rev.* **113,** 3949–3985 (2013).

632 46. Vayssilov, G. N., Mihaylov, M., Petkov, P. S., Hadjiivanov, K. I. & Neyman, K. M.
633 Reassignment of the Vibrational Spectra of Carbonates, Formates, and Related Surface
634 Species on Ceria: A Combined Density Functional and Infrared Spectroscopy Investigation.
635 *J. Phys. Chem. C* **115,** 23435–23454 (2011).

636 47. Bengaard, H. S. *et al.* Steam Reforming and Graphite Formation on Ni Catalysts. *J. Catal.*
637 **209,** 365–384 (2002).

638 48. Grass, M. E. *et al.* New ambient pressure photoemission endstation at Advanced Light
639 Source beamline 9.3.2. *Rev. Sci. Instrum.* **81,** 053106 (2010).

640 49. Frank Ogletree, D., Bluhm, H., Hebenstreit, E. D. & Salmeron, M. Photoelectron
641 spectroscopy under ambient pressure and temperature conditions. *Nucl. Instruments Methods*
642 *Phys. Res. Sect. A Accel. Spectrometers, Detect. Assoc. Equip.* **601,** 151–160 (2009).

643 50. Whaley, J. a. *et al.* Note: Fixture for characterizing electrochemical devices in-operando in
644 traditional vacuum systems. *Rev. Sci. Instrum.* **81,** 1–3 (2010).

645 51. Hwang, W., Kim, Y.-K. & Rudd, M. E. New model for electron-impact ionization cross
646 sections of molecules. *J. Chem. Phys.* **104,** 2956 (1996).

647 52. Balaji Gopal, C. *et al.* Equilibrium oxygen storage capacity of ultrathin $CeO_{2-\delta}$ depends non-
648 monotonically on large biaxial strain. *Nat. Commun.* **8,** 15360 (2017).

649 53. Fabris, S., de Gironcoli, S., Baroni, S., Vicario, G. & Balducci, G. Reply to "Comment on
650 'Taming multiple valency with density functionals: A case study of defective ceria'". *Phys.*
651 *Rev. B* **72,** 237102 (2005).

652 54. Farra, R. *et al.* Promoted Ceria: A structural, catalytic, and computational study. *ACS Catal.*
653 **3,** 2256–2268 (2013).

654 55. Nørskov, J. K., Studt, F., Abild-Pedersen, F. & Bligaard, T. *Fundamental Concepts in*
655 *Heterogeneous Catalysis*. *Fundamental Concepts in Heterogeneous Catalysis* (John Wiley &
656 Sons, Inc, 2014).

657 56. Jensen, S. H., Hauch, A., Hendriksen, P. V. & Mogensen, M. Advanced Test Method of
658 Solid Oxide Cells in a Plug-Flow Setup. *J. Electrochem. Soc.* **156,** B757 (2009).

659 57. Skafte, T. L. *et al.* Data uploaded to Figshare, DOI: 10.11583/DTU.4479050. (2019).

58. Winther, K. T. *et al*. Catalysis-Hub.Org, an Open Electronic Structure Database for Surface Reactions. *Sci. Data* **6**, 75 (2019).

Acknowledgments: We thank Liming Zhang for SEM assistance, Anne Lyck Smitshuysen for assistance with preparing the large-format cells, Rodrigo M. Ortiz de la Morena for 3D modeling and rendering the wind turbine in Fig. 5, and Hendrik Bluhm for assistance at beamline 11.0.2. This research used resources of the Advanced Light Source, which is a DOE Office of Science User Facility under contract no. DE-AC02-05CH11231.

The authors gratefully acknowledge financial support from Haldor Topsoe A/S, Innovation Fund Denmark, the Danish Agency for Science, Technology and Innovation (grant no. 5176-00001B and 5176-00003B), and Energinet.dk under the project ForskEL 2014-1-12231. The work was also supported by the National Science Foundation CAREER Award (1455369). M.B. acknowledges support from by the U.S. Department of Energy, Chemical Sciences, Geosciences, and Biosciences (CSGB) Division of the Office of Basic Energy Sciences, via Grant DE-AC02-76SF00515 to the SUNCAT Center for Interface Science and Catalysis. We thank J. Nørskov and T. Bligaard at SUNCAT Center for Interface Science and Catalysis for hosting T.L.S. and C.G. All calculations in this work were performed with the use of the computer time allocation (m2997) at the National Energy Research Scientific Computing Center, a DOE Office of Science User Facility supported by the Office of Science of the U.S. Department of Energy under Contract No. DE-AC02-05CH11231.

Author contributions: T.L.S, C.G. and W.C.C designed the experiments. T.L.S. carried out the spectroscopic and electrochemical analysis. M.L.M., L.M., E.S., S.S., and T.L.S. manufactured samples. T.L.S., Z.G. and C.G. carried out preliminary experiments and sample characterization. Z.G., T.L.S., C.B.G., M.M, C.G., M.L.M., and E.J.C. carried out the XPS experiments. M.B. and M.G.-M. designed and conducted the DFT calculations. T.L.S. and C.G. carried out the large-format cell experiments. T.L.S., C.G., W.C.C., M.B., M.G.-M., J.A.G.T., Z.G., and M.M. contributed to

writing the article. C.G. initiated the collaborative project. W.C.C and C.G. supervised and guided the work.

Competing interests: Authors declare no competing interests.